2016

Enhanced electron extraction capability of polymer solar cells *via* modifying the cathode buffer layer with inorganic quantum dots

Zhiqi Li
Jilin University

Shujun Li
Jilin University

Zhihui Zhang
Jilin University

Xinyuan Zhang
Jilin University

Jingfeng Li
Jilin University

See next page for additional authors

PCCP

PAPER

View Article Online
View Journal | View Issue

Cite this: *Phys. Chem. Chem. Phys.*, 2016, **18**, 11435

Enhanced electron extraction capability of polymer solar cells *via* modifying the cathode buffer layer with inorganic quantum dots

Zhiqi Li,[a] Shujun Li,[a] Zhihui Zhang,[a] Xinyuan Zhang,[a] Jingfeng Li,[a] Chunyu Liu,[a] Liang Shen,*[ab] Wenbin Guo*[a] and Shengping Ruan[a]

Received 16th February 2016,
Accepted 30th March 2016

DOI: 10.1039/c6cp00989a

www.rsc.org/pccp

Enhanced performance of polymer solar cells (PSCs) based on the blend of poly[*N*-9″-hepta-decanyl-2,7-carbazole-*alt*-5,5-(4′,7′-di-2-thienyl-2′,1′,3′-benzothiadiazole)] (PCDTBT):[6,6]-phenyl-C_{70}-butyric acid methyl ester ($PC_{71}BM$) is demonstrated by titanium dioxide (TiO_2) interface modification *via* $CuInS_2$/ZnS quantum dots (CZdots). Devices with a TiO_2/CZdots composite buffer layer exhibit both a high short-circuit current density (J_{sc}) and fill factor (FF), leading to a power conversion efficiency (PCE) up to 7.01%. The charge transport recombination mechanisms are investigated by an impedance behavior model, which indicates that TiO_2 interfacial modification results in not only increasing the electron extraction but also reducing impedance. This study provides an important and beneficial approach to develop high efficiency PSCs.

1. Introduction

Polymer bulk heterojunction (BHJ) solar cells based on composites of electron-donating polymers and electron-accepting fullerene derivatives exhibit potential advantages in making printable, portable, flexible, and large-area devices with relatively low-cost fabrication and are anticipated to be promising candidates to utilize solar energy.[1–7] Over the last decade, many efforts have been devoted to further improving the performance of polymer solar cells (PSCs), such as designing new device structures and new polymers with enhanced properties and optimizing device morphology.[8–14] However, the overall efficiency of BHJ-PSCs is still limited by many factors. The major drawbacks of BHJ-PSCs are often attributable to the narrow light absorption band of the polymers, low charge carrier mobility and limited exciton migration.[15–20] Especially, a poor electron-extracting capability continues to be a big bottleneck for realizing high efficiency, and many approaches have been developed to improve charge carrier transfer for PSCs.

Recently, inverted structure PSCs with TiO_2 or ZnO as a cathode buffer layer and high work function MoO_3 as the anode buffer layer have attracted great attention because the inverted configuration provides better stability and design flexibility.[21–23] However, the rebellious nanomorphology of the inorganic layer makes it difficult to attain an optimized interface with the polymer layer to enhance interconnected pathways for charge transport, as well as decrease charge recombination. For high performance inverted PSCs, the interfaces between electrodes and active layers should be an ohmic contact to maximize the open-circuit voltage (V_{oc}) and minimize contact resistance. Furthermore, balanced charge transport and collection are basic requirements for highly efficient optoelectronic devices. Hence, various ways have been employed to modify the interfacial layer between the active layer and electrode to enhance charge transport and reduce the interfacial contact resistance.[24,25] However, the choices of these ways used in polymeric materials are limited, as these require good compatibility in solubility, simple fabrication processes, and efficient charge transfer. An available strategy is to enhance the device efficiency by introducing soluble materials into the PSCs. Aqueous soluble inorganic quantum dot materials could also be promising candidates as efficient interface modification materials for highly efficient inverted PSCs,[26] because they have superior charge carrier mobility and could act as exciton dissociation centers, which is beneficial for the future development of all-solution processed PSCs.[27–29]

In this contribution, we investigated the role of the $CuInS_2$/ZnS quantum dots (CZdots) in interfacial modification of TiO_2 for BHJ-PSCs. Impedance spectroscopy (IS) was examined in the dark with different bias voltages (including open-circuit conditions, V_{oc}) to investigate the kinetics and energetic processes

[a] *State Key Laboratory on Integrated Optoelectronics, Jilin University, College of Electronic Science and Engineering, 2699 Qianjin Street, Changchun 130012, People's Republic of China. E-mail: shenliang@jlu.edu.cn, guowb@jlu.edu.cn*
[b] *Department of Mechanical and Materials Engineering and Nebraska Center for Materials and Nanoscience, University of Nebraska–Lincoln, Lincoln, Nebraska 68588-0656, USA*

governing the device performance.[30–33] It is also an available tool to observe bulk and interfacial electrical properties that cannot be directly observed,[34] such as the built-in voltage, doping concentration, diffusion time, and carrier mobility.[35–39] By modelling the impedance behavior to investigate the charge transport recombination mechanisms, it was found that there is efficient charge transfer between TiO_2 and the active layer, leading to improved electron mobility and energy level alignment for PSCs. The results demonstrate that CZdots can act as an efficient additive to improve the electron extraction capacity of BHJ-PSCs.

2. Experimental section

The CZdots nanocrystal (average diameter is about 4.5 nm and the surface ligand is oleic acid) was purchased from NNCrystal Co. Ltd. Poly[*N*-9″-hepta-decanyl-2,7-carbazole-*alt*-5,5-(4′,7′-di-2-thienyl-2′,1′,3′-benzothiadiazole)] (PCDTBT) and [6,6]-phenyl-C_{70}-butyric acid methyl ester ($PC_{71}BM$) were purchased from 1-Material Inc. and Lumtek Corp. without any purification, respectively. To fabricate inverted PSCs, commercial ITO-coated glass substrates were manually washed in acetone, isopropanol, and deionized water respectively. And then, the substrates were blow-dried with nitrogen and dealt with UV ozone for 20 min. The electron transporting layer (TiO_2) was prepared by a sol–gel method, spin-coated at 3000 rotations per minute (rpm) for 20 s and annealed on a muffle furnace. The CZdots material was dissolved in chlorobenzene with a concentration of 2 mg mL^{-1}, and the solution was spin-coated on the surface of the TiO_2 films. The devices modified with CZdots made at 3000, 2000, and 1000 rpm were named as Device B, Device C, and Device D, and the control device without CZdots was Device A. The corresponding film thicknesses of the CZdots layers made at 3000, 2000, and 1000 rpm are 4 nm, 7 nm, and 10 nm respectively, which were measured by an Ellipsometer. The active layer blend of PCDTBT:$PC_{71}BM$ was spin-coated on the CZdots layers and then annealed on a hot plate in a glove box at 70 °C for 20 min, and finally, the photovoltaic devices were finished by thermal evaporation of a thin layer of MoO_3 (4 nm) followed by a Ag electrode (100 nm) with a furnace pressure lower than 10^{-5} Torr,[40–42] and the active layer area of the device was defined by a shadow mask of 3.2 mm × 2 mm, so the device area of the PSCs is 6.4 mm^2. Except for the heat treatment of the active layer films in a glove box, all processes of device fabrication were done in air. All the data on the device performance presented in the article are typical average values of 32 devices from 8 repeated experiments.

3. Results and discussion

The effect of TiO_2/CZdots as an electron transporting layer was investigated with the device structure of ITO/TiO_2/CZdots/PCDTBT:$PC_{71}BM$/MoO_3/Ag, and the device structure and energy levels are shown in Fig. 1a and b respectively. Ultraviolet photoelectron spectroscopy (UPS) and a Kelvin probe system (KP) were combined to study the properties of the CZdots. It is worth noting that the TiO_2/CZdots composite cathode buffer layer has a decreased work function compared to that of the pristine TiO_2 film (Fig. 1c). As shown in Fig. 2a, UPS was used to measure the surface chemical composition and energy levels of the nanocrystals. The ultraviolet excitation energy (U_e) is 21.22 eV, where $E_{LUMO} = U_e - (E_2 - E_1)$. E_1 is the side of the boundary on

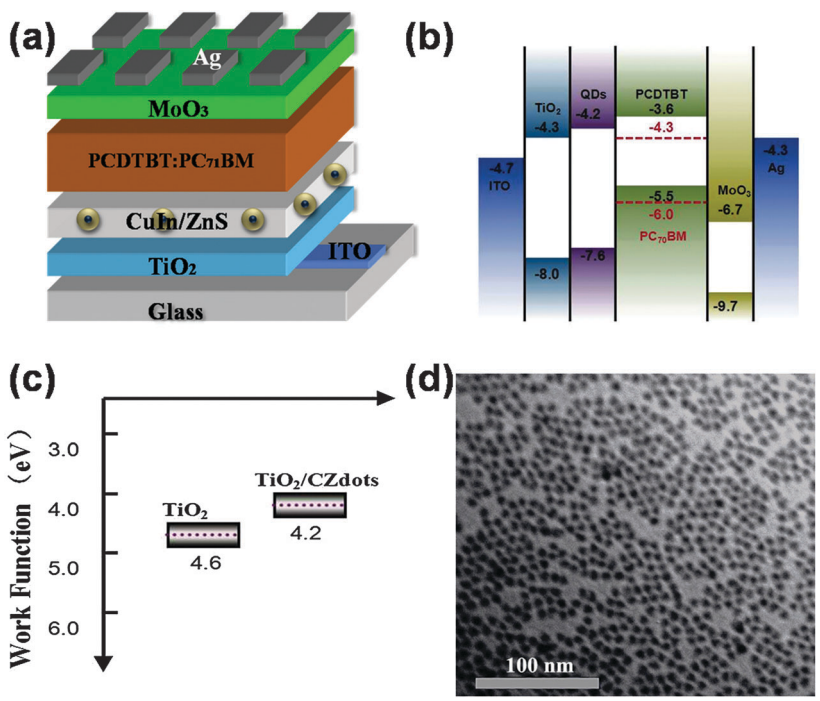

Fig. 1 (a) The device structure of the inverted PSCs, (b) the scheme of energy levels of all materials used in the study, (c) the work function of TiO_2 and TiO_2/CZdots, and (d) TEM image of the CZdots layer on TiO_2.

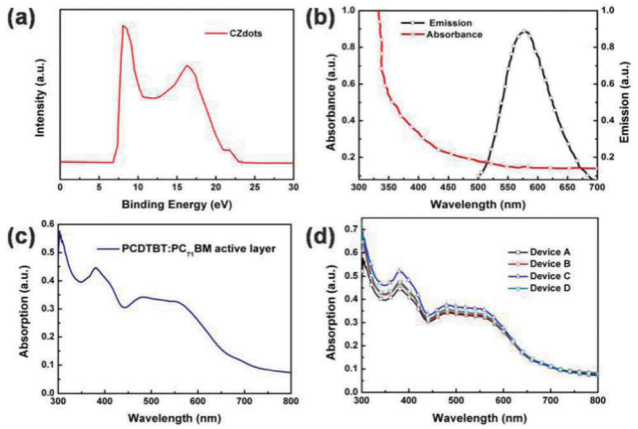

Fig. 2 (a) UPS image of the CZdots/TiO_2 film, (b) the absorption and emission spectra of the CZdots, (c) the absorption spectrum of the active layer, and (d) the absorption image of the completed devices.

the left and E_2 is on the right in Fig. 2a. The results indicate that the CZdots precursor solution spin-coating on TiO_2 substrates with proper temperature annealing, CZdots with a lowest unoccupied molecular orbital (LUMO) of 4.0 eV and a highest occupied molecular orbital (HOMO) of 7.6 eV have been formed,[43–45] which is included in Fig. 1b. The work function of the CZdots was measured with a value of 4.2 eV, which matches well with the work function of TiO_2 and the LUMO of $PC_{71}BM$. In fact, the core/shell structure uniform distribution CZdots layer (Fig. 1d) plays a key role in electron transport from $PC_{71}BM$ to TiO_2. As a result, this work function tuning by interfacial layers provides efficient charge collection centers and remarkably accelerates charge transfer rates from excited organic molecules to inorganic materials. Furthermore, the absorption and emission spectra of the CZdots are also located in the ultraviolet and visible region (Fig. 2b), and active layer absorption is presented in Fig. 2c, which shows that the emission spectrum of the CZdots is partially overlapping with the absorption area of the active layer. All of these increase the utilization of ultraviolet photons, which accounts for the enhancement of photon absorption for the PSCs (Fig. 2d). In order to prove the photovoltaic performance of the CZdots, Fig. 3a displays the representative current density *versus* voltage (*J–V*) characteristics, recording the performance of the PSCs prepared using a TiO_2 buffer layer with and without CZdots modification, and the corresponding photovoltaic average parameters of 32 devices are summarized in Table 1. It is noted that the device without the CZdots sensitized layer exhibited a relatively low efficiency, including a short-circuit current (J_{sc}) of 12.73 mA cm^{-2}, an open-circuit voltage (V_{oc}) of 0.86 V, a fill factor (FF) of 52.54%, and a calculated PCE of 5.72%. However, after the CZdots additive was employed to modify the TiO_2 interfacial layer, Device C shows a significant improvement with a J_{sc} of 14.04 mA cm^{-2}, a V_{oc} of 0.86, and a FF of 57.77%, leading to an increased PCE up to 7.01%, which is presented in Table 1. Observably, the surface treatment devices with an x nm thick CZdots sensitization layer show a gradually improved performance, and the optimal thickness is x = 7 nm. It is also found that the device performance is highly sensitive to the thickness of the CZdots layer attached on the TiO_2 buffer layer, and the performance enhancement is ascribed to electron extraction capability improvement. Meanwhile, it can also be seen that the values of the V_{oc} for the devices treated with CZdots have changed little compared to that of the control device, suggesting that CZdots have no effect on the built-in potential.

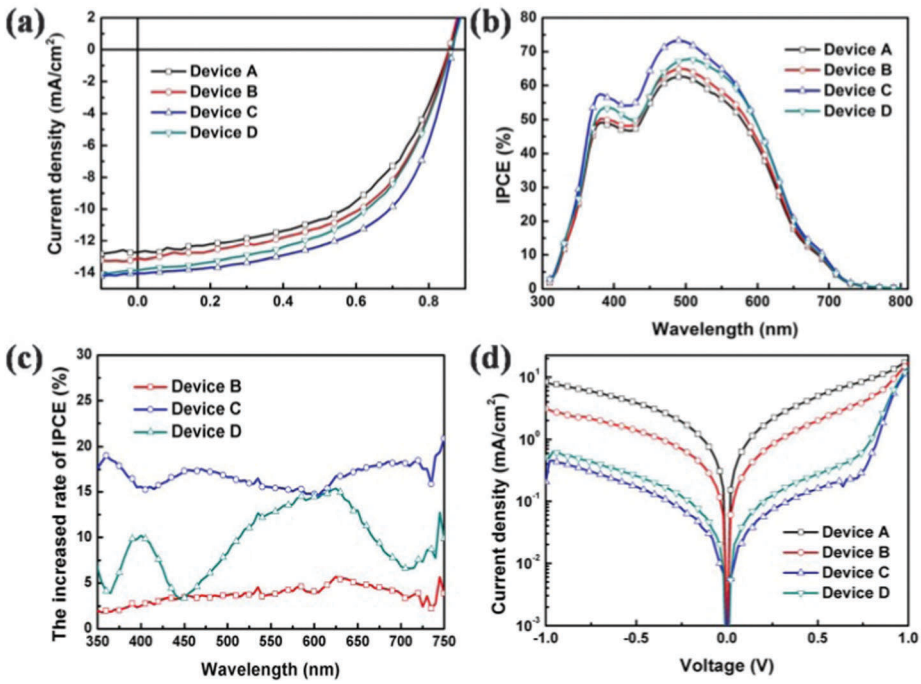

Fig. 3 (a) *J–V* characteristics of the solar cells without and with different thicknesses of CZdots, (b) IPCE spectra of all devices, (c) increasing rate of IPCE for the optimized devices, and (d) *J–V* characteristics of all the photovoltaic devices in the dark.

Table 1 The detailed photovoltaic parameters of all the PSCs without and with various thicknesses of CZdots

Device	V_{oc} (V)	J_{sc} (mA cm^{-2})	FF (%)	PCE (%)	R_s (Ω)	R_{sh} (Ω)
A	0.86	12.73	52.50	5.96	224.14	4807.54
B	0.86	13.10	54.67	6.27	183.92	3764.41
C	0.87	14.04	57.77	7.19	133.38	24981.2
D	0.86	13.84	52.87	6.50	198.81	6757.36

To deeply investigate the mechanism of the J_{sc} increase, the incident photon-to-electron conversion efficiency (IPCE) of the devices with and without the CZdots modifier was tested, and the obtained spectra are exhibited in Fig. 3b. As expected, the IPCE variation indicates a good agreement with the J–V characteristics. Meanwhile, the IPCE of the devices modified with various thicknesses of CZdots shows a significant enhancement in a broad wavelength region of 375–750 nm compared to the control device, providing direct evidence for the gradually increased J_{sc}. The IPCE results also clearly reveal that the improvement of device performance is sensitive to the thickness of CZdots on the TiO_2 surface, and Device C exhibits the highest photon-to-electron conversion efficiency due to the strongest electron transport capacity from the 7 nm CZdots film. The IPCE difference data of the sensitized devices and the control device are shown in Fig. 3c, which is calculated by $R = (\mathrm{IPCE_{CZdots\ device}} - \mathrm{IPCE_{Control\ device}})/\mathrm{IPCE_{Control\ device}}$. In order to further certify the J_{sc} and FF increase, the dark J–V characteristics of the PSCs are displayed in Fig. 3d. The modified devices with CZdots interfacial layers exhibit a smaller leakage current at a negative voltage and a low positive voltage, and the dark J_{sc} increases sharply at a high positive voltage, resulting in a high rectifying ratio of the diodes. The improved dark J_{sc} characteristics lead to a decrease of the series resistance and an increase of shunt resistance, contributing to the enhancement of the FF and PCE. The statistical histograms of the photovoltaic parameters for the control and the best optimized devices are exhibited in Fig. 4, and the V_{oc}, J_{sc}, FF, and PCE results are included in Fig. 4a–d.

To gain more insight into the role of the CZdots layer on the mechanism of charge recombination and transport process for the control and optimal devices, the dependence of the photocurrent density (J_{ph}) on the effective voltage (V_{eff}) on a double-logarithmic scale is indicated in Fig. 5, which was obtained without and with illumination of 100 mW cm^{-2}. Herein, $J_{ph} = J_L - J_D$, and J_L and J_D are the current densities under illumination and in the dark, respectively. Simultaneously, $V_{eff} = V_o - V$, V is the applied voltage, and V_o is the compensation voltage at $J_{ph} = 0$.[46] J_{ph} increases linearly with the effective voltage (V_{eff}) when V_{eff} is less than 0.3 V, and the slope shows that the maximum exciton generation rates (G_{max}) of the sensitized solar cells are higher than that of the control device. It is worth noting that J_{ph} increases faster with V_{eff} in the optimized devices, which implies a faster rate of absorbed photons to electrons. Especially, interface modification increases the electron transport and collection, hence the response speed of the sensitized devices becomes faster, leading to an enhanced exciton dissociation probability ($P(E,T)$). $P(E,T)$ was calculated by normalized processing: $P(E,T) = J_{ph}/J_{sat}$, where J_{sat} is the

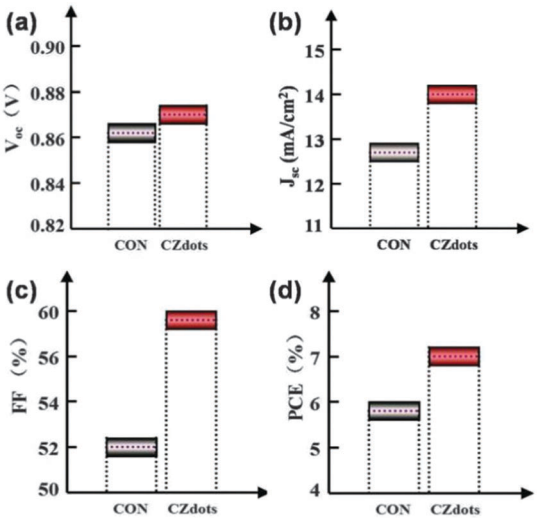

Fig. 4 The data histograms for the control device and the best devices.

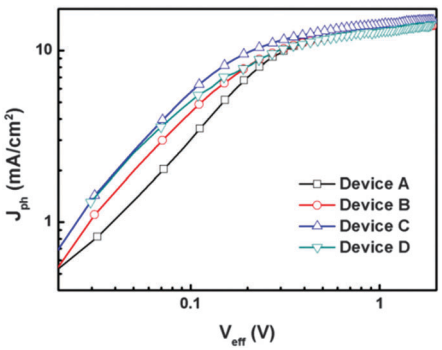

Fig. 5 Photocurrent density (J_{ph}) as a function of the effective voltage (V_{eff}) for the control device and CZdots device.

saturation photocurrent density. Fig. 5 shows that J_{ph} tends to saturate at a sufficiently high value ($V_{eff} > 1$ V), and the higher J_{ph} value usually implies a higher charge extraction efficiency,[47] accounting for a relatively increased FF and J_{sc} for the modified devices. J_{sat} can be deduced from Fig. 5, which is only related to the absorbed incident photon flux and is independent of the bias and temperature. All of these characteristics are reflected in the advanced IPCE present in Fig. 3b, and the modified devices show higher IPCE values across the entire wavelength region from 300 to 800 nm compared to the reference device. The maximum IPCE values for the optimally modified and the control devices are 75% and 63% at 480 nm respectively, which match with the J_{sc} trend well.

It is widely recognized that the nanomorphology of the films plays a crucial role in the charge separation and transport process for organic photovoltaic devices. The influence of surface modification on the TiO_2 buffer layer by CZdots was examined by atomic force microscopy (AFM). Fig. 6 shows the AFM topographic images of bare TiO_2 films as well as the TiO_2/CZdots films with different thicknesses. For Device C, it shows a very smooth and featureless structure with a low root-mean-square (RMS) value of 0.96 nm. However, the RMS values slightly increased to

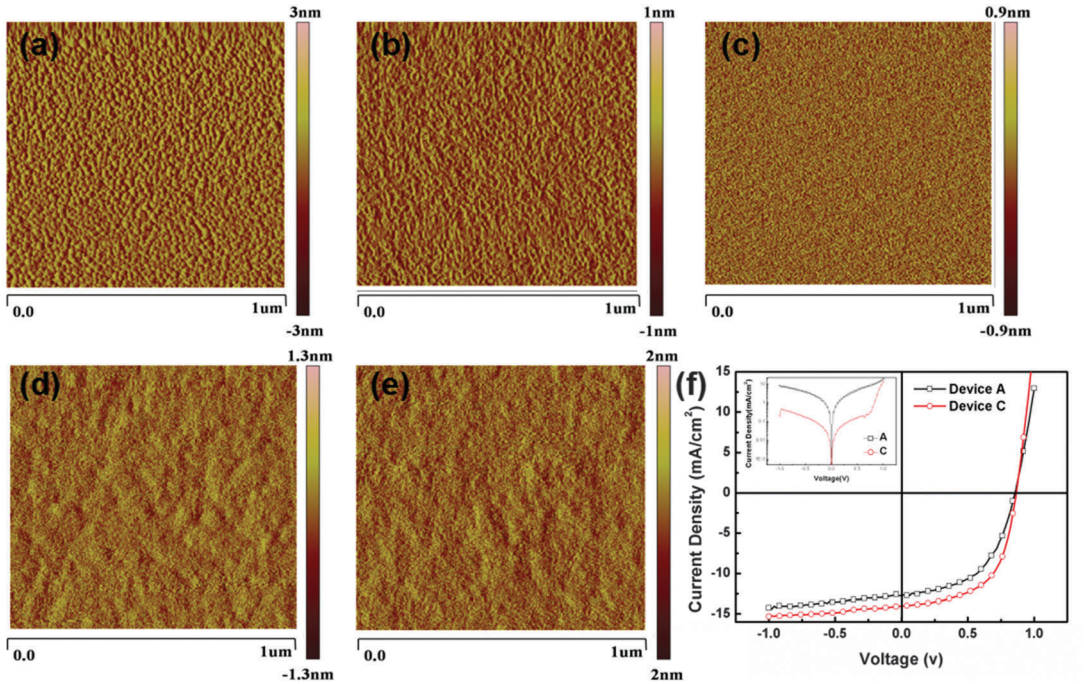

Fig. 6 AFM morphology image of the TiO_2/CZdots films: (a) pristine TiO_2 film, (b) 4 nm CZdots layer, (c) 7 nm CZdots layer, (d) 10 nm CZdots layer, and (e) 15 nm CZdots layer. (f) *J–V* characteristics of the control and optimized cells under illumination and in the dark (inset).

5.54 nm (Device A), 1.04 nm (Device B), 1.37 nm (Device D), and 1.83 nm (CZdots film made under 500 rpm), respectively. It means that surface modification with CZdots changes the roughness of the TiO_2 cathode buffer layers. The minor variation of the film morphology would have a significant impact on charge transfer, and the smooth and featureless interface improves the electron transport and collection. The introduction of CZdots facilitates the electron injection and smaller charge recombination probabilities in the interface. Therefore, it is reasonable to speculate that the electron transport property will be energetically favored at the TiO_2/CZdots interface, which is confirmed by the J_{sc} enhancement of the modified devices (Fig. 6f). Interfacial modification of the CZdots layer results in a very smooth nanomorphology and smaller domain sizes of the surface. We conclude that the decrease of interfacial crystallinity and the formation of smaller nanoscale domains lead to two possible results. On the one hand, the smaller sizes of TiO_2/CZdots in comparison with referenced TiO_2 would result in a better interfacial contact, hence a reduced interface trap, decreased interfacial recombination and enhanced diffusion rate in the process of electron transport. On the other hand, due to the interaction between TiO_2/CZdots and the PCDTBT:$PC_{71}BM$ blend at the interface, the modification of CZdots may serve as boundary transport nucleus centers for electron transfer compared to the control device, thus leading to improved electron mobility and decreased energy loss. Additionally, besides the smaller charge recombination at the TiO_2/CZdots interface through the improved morphology, CZdots also serve as an extra electron transport medium between TiO_2 and the active layer.

Generally, efficient interfacial modification usually leads to lower resistance for photovoltaic devices, and the series resistance greatly affects the *J–V* characteristics of the PSCs. The *J–V* equation of the PSCs is usually modeled by means of a behavior as:[48,49]

$$j = \frac{1}{1+\frac{R_s}{R_p}}\left\{ j_0\left[\exp\left(\beta\frac{V_{app}-jR_s}{k_B\frac{T}{q}}\right)\right] - 1 - \left[J_{ph}-\frac{V_{app}}{R_p}\right]\right\} \quad (1)$$

where V_{app} is the applied voltage, and J_{ph} accounts for the photocurrent, which is reduced by the shunt resistance R_p. Besides, k_{BT} stands for the thermal energy, q is the elementary charge, j_0 represents the dark current, and the parameter β accounts for the deviation from the diode ideal equation (inverse of the diode ideality factor). Therefore, an equivalent circuit diagram for the actual blending system of the organic solar cell in the actual test has been given, from which different circuit elements for the actual factors can be derived. As shown in Fig. 7a, C_μ is the chemical capacitance (connected to carrier storage), R_{rec} is the recombination resistance (derivative of the carrier recombination flux) response, R_1 is the transport-related resistance, C_1 is related to geometrical and dielectric mechanisms, and R_0 is the anode interface, buffer layer, and wire resistance for the PSCs.[50] The series resistance (R_s) was introduced as $R_s = R_1 + R_0$. It can be seen from Table 1 that R_s significantly tends to decrease due to the incorporation of CZdots, resulting in an increased FF.

Fig. 8 presents the Nyquist plots of the impedance spectra for the control and modified devices at different thicknesses of CZdots at the open-circuit applied voltage. These semicircles can help us to understand the internal resistance of the different modified devices. From the impedance spectra, it clearly depicts that the semicircle's diameter for the reference devices is much larger than that of the modified devices. It demonstrates the

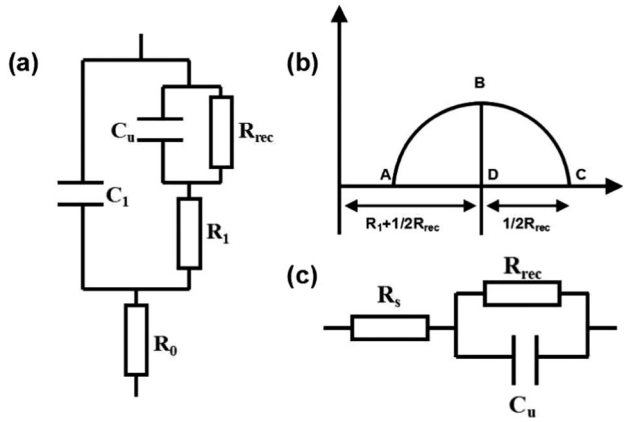

Fig. 7 (a) Equivalent circuit diagram for the actual blending system of the PSCs, (b) impedance spectra for the simplified circuit of the PSCs, and (c) simplified circuit diagram for the actual blending system of the PSCs.

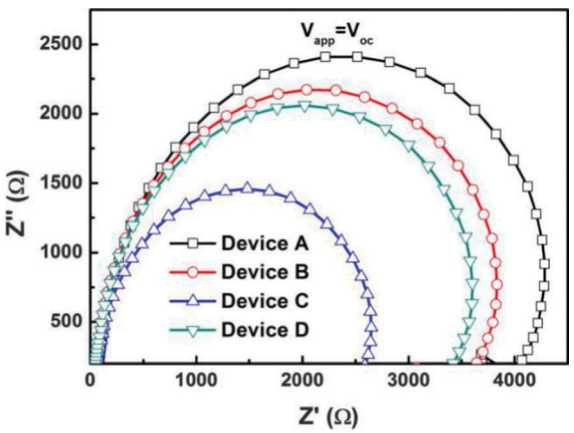

Fig. 8 Impedance spectra of the PSCs with different thicknesses of CZdots under open-circuit conditions.

recombination resistance of the CZdots modified devices is apparently decreased. Meanwhile, as shown in Table 1, the calculated series resistance from the *J*–*V* curve is obviously reduced, which contributes to the increase of the J_{sc} and FF. And a higher capacitance is obtained after interfacial modification with CZdots, resulting in a higher electron concentration.

These experimental data resemble the typical semicircle shape, which can be accurately modeled with a simple parallel RC circuit (Fig. 7c). The imaginary part and real part in Fig. 7b, mapped as a semicircle in the coordinate axes, are related to the resistance:[51–53]

$$Z = R_1 + \frac{1}{\frac{1}{R_r} + j\omega C_\mu} \quad (2)$$

or

$$Z = R_1 + \frac{R_r}{1+\omega R_r C_d} - j\frac{\omega R_r^2 C_\mu}{1+(\omega R_r C_\mu)^2} \quad (3)$$

The data of the center coordinates of the circle formulate ($x = R_1 + R_r/2$, $y = 0$), and R_1, R_r and C_μ can be given by the following equations:

$$OA = R_1 \quad (4)$$

$$AC = R_r \quad (5)$$

$$C_\mu = 1/\omega_B R \quad (6)$$

$$i_0 = RT/nFR_r \quad (7)$$

The capacitance C_μ is attributed to the depletion region chemical capacitance due to connecting to the carrier storage.[54] This capacitance follows the Mott–Schottky expression:

$$C_\mu^{-2} = \frac{2(V_{bi}-V)}{A^2 e\varepsilon_0\varepsilon_D N} \quad (8)$$

and

$$V_{bi} = \phi_{bi} + \frac{KT}{e} \quad (9)$$

where V_{bi} is the built-in potential, N is the impurity density, A is the area (6.4 mm^2 in this paper), V is the applied voltage, and ε_A and ε_0 are the dielectric constant and vacuum permittivity, respectively. In order to explore the role of the CZdots interfacial layer on the device performance improvement, the capacitance–voltage characteristics of the devices were measured and compared to the result obtained from the Mott–Schottky relation. The charge carrier density can be calculated by:

$$N = \frac{1}{e}Ad\int_{dark}^{V_{oc}} C(V)\mathrm{d}V \quad (10)$$

where e is elementary charge, A is the device area, d is the thickness of the active layer, and C is the chemical capacitance. The chemical capacitance is simulated using the Schottky equivalent circuit model and following the Mott–Schottky expression. Fig. 9 shows the impedance spectra of all the devices at different voltage values. From the impedance spectra, we extracted C_μ and the carrier concentration (ND) from the linear region. For the optimized device (Fig. 9c), the average electron number is around 1.81×10^{15}, which is slightly higher than that obtained from the control device (1.62×10^{15} calculated from Fig. 9a). We also calculated the carrier concentrations for Device B (Fig. 9b) and

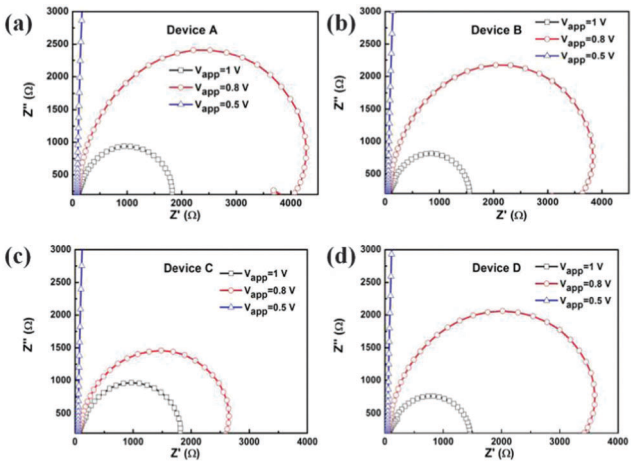

Fig. 9 Impedance spectra of (a) Device A, (b) Device B, (c) Device C, and (d) Device D at different applied voltage values, respectively.

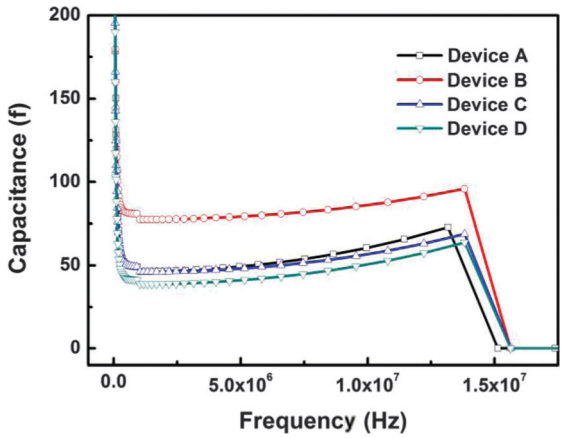

Fig. 10 Capacitance–frequency characteristics of all the fabricated devices.

Device D (Fig. 9d), which are also smaller than that of the optimized device. Except for the improved morphology, CZdots can be considered as an efficient electron transfer center, and CZdots could accelerate efficient exciton dissociation at the active layer interface. Likewise, it is reasonable to speculate that exciton dissociation would be energetically favored at the PCDTBT:$PC_{71}BM$ and TiO_2 interface, which is confirmed by the increased electron number from the reference device to the optimal modified device.

The equivalent circuit diagram for the PSCs in the actual test shows that a capacitor connects the anode and the cathode. In fact, the AC voltage as a modulating signal is applied to the electrodes of the PSCs, which induces current carrying across the devices. This results in a capacitor-like device that stores and releases energy quickly. Thus, the electron mobility can be calculated from this process. In order to further probe the transport recombination mechanism for the optimized devices, admittance spectroscopy was measured to get the electron mobility and carrier transit time. Fig. 10 presents the capacitance–frequency characteristics of the solar cells; we found that the cell capacitance rapidly changed with increasing frequency. As we know, frequency is another way of representing the carrier transit time for most of the carrier current (τ_r), and the mean transit time (τ_r) can be calculated. Therefore, the electron mobility can be extracted from the equation:

$$\mu_{dc} = \frac{d}{(\tau_{dc} V_{dc})} \quad (11)$$

and

$$\tau_{dc} = 0.56\tau_r \quad (12)$$

where d is the thickness of the polymer and V_{dc} is the external applied bias voltage.[55] Compared to the control devices, the storing and releasing energy of the capacitor for the optimized devices is quicker with enhanced transporting time. Accordingly, the time of storing and releasing for the control device is about 7.6×10^{-8} s, while that of the optimal device is 7.2×10^{-8} s. According to eqn (10), the electron mobility can be obtained. For example, when the typical bias V_{dc} is 10 V and d is 100 nm, the electron mobility is increased from 2.35×10^{-3} cm^2 V^{-1} s^{-1} for the control device to 2.46×10^{-3} cm^2 V^{-1} s^{-1} for the optimal device.[56,57] Therefore, besides the facilitated exciton dissociation through improved morphology, CZdots can also serve as an extra electron transport medium, leading to enhanced efficient exciton dissociation and electron collection.

4. Conclusions

In summary, a CZdots interface modified layer on TiO_2 plays a significant role on the J_{sc} and FF, leading to a great PCE enhancement. The feature of CZdots was studied using UPS and KP, and the effect of TiO_2 interfacial modification *via* CZdots is demonstrated by the spectroscopy techniques and AFM. The application of CZdots interfacial modification changes the roughness of the electron transporting layer, resulting in a high electron mobility. Improved nanostructures of the TiO_2 surface decrease interfacial charge traps between the active layer and TiO_2, achieving a smaller charge recombination probability. Furthermore, CZdots can also serve as efficient charge transport channels to accelerate electron collection. This study demonstrates an effective approach to optimize the performance of PSCs using quantum dot materials.

Acknowledgements

The authors are grateful to the National Natural Science Foundation of China (61275035, 61370046, 11574110), Project of Science and Technology Development Plan of Jilin Province (20130206075SF), and the Opened Fund of the State Key Laboratory on Integrated Optoelectronics (IOSKL2013KF10).

Notes and references

1 M. Andersen, J. E. Carle, N. Cruys-Bagger, M. R. Lilliedal, M. A. Hammond, B. Winther-Jensn and F. C. Krebs, *Sol. Energy Mater. Sol. Cells*, 2007, **91**, 539.
2 H. H. Liao, L. M. Chen, Z. Xu, G. Li and Y. Yang, *Appl. Phys. Lett.*, 2008, **92**, 173303.
3 C. Waldauf, M. Morana, P. Denk, P. Schilinsky, K. Coakley, S. A. Choulis and C. J. Brabec, *Appl. Phys. Lett.*, 2006, **89**, 233517.
4 K. S. Lee, J. A. Lee, B. A. Mazor and S. R. Forst, *Light: Sci. Appl.*, 2015, **4**, e288.
5 E. D. Kosten, J. H. Awater, J. Parsons, A. Polman and H. A. Awater, *Light: Sci. Appl.*, 2013, **2**, e45.
6 S. K. Hau, H. L. Yip, N. S. Baek, J. Zou, K. O'Malley and A. K. Y. Jen, *Appl. Phys. Lett.*, 2008, **92**, 253301.
7 C. F. Guo, T. S. Sun, F. Gao, Q. Liu and Z. F. Ren, *Light: Sci. Appl.*, 2014, **3**, e161.
8 J. B. You, L. T. Dou, K. Yoshimura, T. Kato, K. Ohya, T. Moriarty, K. Emery, C. C. Chen, J. Gao, G. Li and Y. Yang, *Nat. Commun.*, 2013, **4**, 1446.
9 Z. C. He, C. M. Zhong, S. J. Su, M. Xu, H. B. Wu and Y. Cao, *Nat. Photonics*, 2012, **6**, 591.

10 X. N. Yang, J. Loos, S. C. Veenstra, W. J. H. Verhees, M. M. Wienk, J. M. Kroon, M. A. J. Michels and R. A. J. Janssen, *Nano Lett.*, 2005, **5**, 579.
11 G. Dennler, M. C. Scharber and C. J. Brabec, *Adv. Mater.*, 2009, **21**, 1323.
12 J. K. Lee, W. L. Ma, C. J. Brabec, J. Yuen, J. S. Moon, J. Y. Kim, K. Lee, G. C. Bazan and A. J. Heeger, *J. Am. Chem. Soc.*, 2008, **130**, 3619.
13 J. Peet, J. Y. Kim, N. E. Coates, W. L. Ma, D. Moses, A. J. Heeger and G. C. Bazan, *Nat. Mater.*, 2007, **6**, 497.
14 S. Khodabakhsh, B. M. Sanderson, J. Nelson and T. S. Jones, *Adv. Funct. Mater.*, 2006, **16**, 95.
15 B. C. Park, S. H. Yun, C. Y. Cho, Y. C. Kim, J. C. Shin, H. G. Jeon, Y. H. Huh, I. C. Hwang, K. Y. Baik and Y. I. Lee, *Light: Sci. Appl.*, 2014, **3**, e222.
16 Z. C. He, C. M. Zhong, X. Huang, W. Y. Wong, H. B. Wu, L. W. Chen, S. J. Su and Y. Cao, *Adv. Mater.*, 2011, **23**, 4636.
17 L. Y. Lu, T. Xu, W. Chen, J. M. Lee, Z. Q. Luo, I. H. Jung, H. I. Park, S. O. Kim and L. P. Yu, *Nano Lett.*, 2013, **13**, 2365.
18 X. Chen, B. H. Jia, Y. A. Zhang and M. Gu, *Light: Sci. Appl.*, 2013, **2**, e92.
19 Z. C. Holman, S. D. Wolf and C. Ballif, *Light: Sci. Appl.*, 2013, **2**, e106.
20 Y. H. Su, Y. F. Ke, S. L. Cai and Q. Y. Yao, *Light: Sci. Appl.*, 2012, **1**, e14.
21 G. Li, C. W. Chu, V. Shrotriya, J. Huang and Y. Yang, *Appl. Phys. Lett.*, 2006, **88**, 253503.
22 P. D. Li, T. G. Jiu, G. Tang, G. J. Wang, J. Li, X. F. Li and J. F. Fang, *ACS Appl. Mater. Interfaces*, 2014, **6**, 18172.
23 G. J. Wang, T. G. Jiu, G. Tang, J. Li, P. D. Li, X. J. Song, F. S. Lu and J. F. Fang, *ACS Sustainable Chem. Eng.*, 2014, **2**, 1331.
24 X. W. Zhan, Z. A. Tan, B. Domercq, Z. S. An, X. Zhang, S. Barlow, Y. F. Li, D. B. Zhu, B. Kippelen and S. R. Marder, *J. Am. Chem. Soc.*, 2007, **129**, 7246.
25 F. Zhang, M. Ceder and O. Inganäs, *Adv. Mater.*, 2007, **19**, 1835.
26 C. Chen and F. M. Li, *Nanoscale Res. Lett.*, 2013, **8**, 453.
27 S. I. Na, T. S. Kim, S. H. Oh, J. Kim, S. S. Kim and D. Y. Kim, *Appl. Phys. Lett.*, 2010, **97**, 223305.
28 G. Cheng, W. Y. Tong, K. H. Low and C. M. Che, *Sol. Energy Mater. Sol. Cells*, 2012, **103**, 164.
29 S. I. Na, S. H. Oh, S. S. Kim and D. Y. Kim, *Org. Electron.*, 2009, **10**, 496.
30 J. Bisquert, E. Palomares and C. A. Quinones, *J. Phys. Chem. B*, 2006, **110**, 19406.
31 I. Mora-Seró, G. García-Belmonte, P. P. Boix, M. A. Váquez and J. Bisquert, *Energy Environ. Sci.*, 2009, **2**, 678.
32 R. A. Kumar, M. S. Suresh and J. Nagaraju, *Sol. Energy Mater. Sol. Cells*, 2000, **60**, 155.
33 G. García-Belmonte, P. P. Boix, J. Bisquert, M. Sesolo and H. J. Bolink, *Sol. Energy Mater. Sol. Cells*, 2010, **94**, 366.
34 T. Ripolles-Sanchís, A. Guerrero, J. Bisquert and G. García-Belmonte, *J. Phys. Chem. C*, 2012, **116**, 16925.
35 T. Kuwabara, C. Iwata, T. Yamaguchi and K. Takahashi, *ACS Appl. Mater. Interfaces*, 2010, **2**, 2254.
36 O. Blum and N. T. Shaked, *Light: Sci. Appl.*, 2015, **4**, e322.
37 D. Lepage, A. Jimenez, J. Beauvais and J. J. Dubowski, *Light: Sci. Appl.*, 2012, **1**, e28.
38 G. H. Kim, H. K. Song and J. Y. Kim, *Sol. Energy Mater. Sol. Cells*, 2011, **95**, 1119.
39 G. Perrier, R. de Bettignies, S. Berson, N. Lemaitre and S. Guillerez, *Sol. Energy Mater. Sol. Cells*, 2012, **101**, 210.
40 B. V. K. Naidu, J. S. Park, S. C. Kim, S. M. Park, E. J. Lee, K. J. Yoon, S. J. Lee, J. W. Lee, Y. S. Gal and S. H. Jin, *Sol. Energy Mater. Sol. Cells*, 2008, **92**, 397.
41 X. C. Li, F. X. Xie, S. Q. Zhang, J. H. Hou and W. C. Choy, *Light: Sci. Appl.*, 2015, **4**, e273.
42 V. D. Mihailetchi, J. Wildeman and P. W. M. Blom, *Phys. Rev. Lett.*, 2005, **94**, 126602.
43 P. W. M. Blom, V. D. Mihailetchi, L. J. A. Koster and D. E. Markov, *Adv. Mater.*, 2007, **19**, 1551.
44 H. L. Yip, S. K. Hau, N. S. Ma, H. Baek and A. K. Y. Jen, *Adv. Mater.*, 2008, **20**, 2376.
45 T. T. Do, H. S. Hong, Y. E. Ha, J. Y. Park, Y. C. Kang and J. H. Kim, *ACS Appl. Mater. Interfaces*, 2015, **7**, 3335.
46 J. D. Chen, C. H. Cui, Y. Q. Li, L. Zhou, Q. D. Ou, C. Li, Y. F. Li and J. X. Tang, *Adv. Mater.*, 2015, **27**, 1035.
47 R. A. Street, K. W. Song and S. R. Cowan, *Org. Electron.*, 2011, **12**, 244.
48 G. García-Belmonte, A. Munar, E. M. Barea, J. Bisquert, I. Ugarte and R. Pacios, *Org. Electron.*, 2008, **9**, 847.
49 B. Arredondo, B. Romero, G. Del Pozo, M. Sessler, C. Veit and U. Würfel, *Sol. Energy Mater. Sol. Cells*, 2014, **128**, 351.
50 G. Garcia-Belmonte, P. P. Boix, J. Bisquert, M. Sessolo and H. J. Bolink, *Sol. Energy Mater. Sol. Cells*, 2010, **94**, 366.
51 Y. B. Xiao, H. Wang, S. Zhou, K. Y. Yan, Z. Q. Guan, S. W. Tsang and J. B. Xu, *ACS Appl. Mater. Interfaces*, 2015, **7**, 13415.
52 W. L. Leong, S. R. Cowan and A. J. Heeger, *Adv. Energy Mater.*, 2011, **1**, 517.
53 Y. Zhang, X. D. Dang, C. Kim and T. Q. Nguyen, *Adv. Energy Mater.*, 2011, **1**, 610.
54 G. García-Belmonte, A. Munar, E. M. Barea, J. Bisquert, I. Ugarte and R. Pacios, *Org. Electron.*, 2008, **9**, 847.
55 D. C. Tripathi, A. K. Tripathi and Y. N. Mohapatra, *Appl. Phys. Lett.*, 2011, **98**, 033304.
56 S. W. Tsang, S. C. Tse, K. L. Tong and S. K. So, *Org. Electron.*, 2006, **7**, 474.
57 S. W. Tsang, S. K. So and J. B. Xu, *J. Appl. Phys.*, 2006, **99**, 013706.

